Springer

Acta Mechanica Sinica

CrossMark click for updates

• RESEARCH PAPER •

Acta Mech. Sin., Vol. 41, 424488 (2025)
https://doi.org/10.1007/s10409-024-24488-x

Atomic lattice-mimic design and optimization of the auxetic metamaterial inspired by the Ti crystal

Jiahui Zhou[1], Yuhang Liu[1], Zunyi Deng[1], Xingang Jiang[1], Wenhao Xiao[1], Bo Yu[1], Yingzhuo Lun[1], Li Meng[2], Gang Tang[3], Zhong Zhang[4], Hongshuai Lei[4], Zewei Hou[1,5*], and Jiawang Hong[1,5*]

[1] *School of Aerospace Engineering, Beijing Institute of Technology, Beijing 100081, China;*
[2] *The School of Physics, Beijing Institute of Technology, Beijing 100081, China;*
[3] *Advanced Research Institute of Multidisciplinary Science, Beijing Institute of Technology, Beijing 100081, China;*
[4] *Institute of Advanced Structure Technology, Beijing Institute of Technology, Beijing 100081, China;*
[5] *Beijing Institute of Technology (Zhuhai), Zhuhai 519088, China*

Received September 12, 2024; accepted September 23, 2024; published online December 27, 2024

Auxetic metamaterials have attracted much attention due to their outstanding advantages over traditional materials in terms of shear capacity, fracture resistance, and energy absorption. However, there are lack of design inspirations for novel auxetic structures. According to the materials databases of atomic lattice, some natural crystals possess negative Poisson's ratio (NPR). In this paper, the mechanism of auxeticity in microscale Ti crystal is investigated through density functional theory simulation. Then we propose a macroscopic auxetic metamaterial by mimicking the microscopic atomic lattice structure of the body-centered cubic Ti crystal. The NPR property of the macroscopic metamaterial is verified by theoretical, numerical and experimental methods. The auxeticity keeps effective when scaling up to macroscopic Ti crystal-mimic structure, with the similar deformation mechanism. Furthermore, from the geometric parameter investigation, the geometric parameters have great influence on the Poisson's ratio and Young's modulus of the macroscopic metamaterial. Importantly, an optimized structure is obtained, which exhibits 2 times enhancement in auxeticity and 25 times enhancement in normalized Young's modulus, compared to the original architecture. This work establishes a link between the physical properties at micro-nanoscale and macroscale structures, which provides inspirations for high load-bearing auxetic metamaterials.

Auxetic metamaterials, Atomic lattice-mimic design, Optimization of metamaterial

Citation: J. Zhou, Y. Liu, Z. Deng, X. Jiang, W. Xiao, B. Yu, Y. Lun, L. Meng, G. Tang, Z. Zhang, H. Lei, Z. Hou, and J. Hong, Atomic lattice-mimic design and optimization of the auxetic metamaterial inspired by the Ti crystal, Acta Mech. Sin. 41, 424488 (2025), https://doi.org/10.1007/s10409-024-24488-x

1. Introduction

Mechanical metamaterials have attracted great interest due to their unconventional characteristics [1-4], such as negative Poisson's ratio (NPR) [5,6], negative stiffness [7], high shear capacity [8], and sound insulation [9]. Auxetic metamaterials possess NPR, which implies that they expand or contract transversely in response to longitudinal tension or compression. Auxetic materials show a number of distinctive mechanical properties, including exceptional shear resistance [10], fracture resistance [11], indentation resistance [12], vibration isolation [13], energy absorption [14], and synclastic behavior [15], etc. Thus, auxetic metamaterials have a wide range of important applications in biomedical materials, smart sensors, aerospace, and actuators [16-18], etc. In the macroscale, several kinds of auxetic mechanisms have been discovered and the corresponding auxetic elements have been designed, including re-entrant structures [19,20], rotating polygons [21-23], chiral structures [24-26], and perforated sheets [16,27]. However, most auxetic metamaterials are obtained by the combination or

*Corresponding authors. E-mail addresses: houzw2022@bit.edu.cn (Zewei Hou); hongjw@bit.edu.cn (Jiawang Hong)
Executive Editor: Shujuan Hou

modification [28-30] of these limited auxetic elements. Design inspiration for novel auxetic structures is needed.

In microscale, some natural crystals can also exhibit unusual physical properties, such as NPR [31,32], negative thermal expansion [33,34] and piezoelectricity [35,36]. Novel deformation mechanisms of these crystal structures may provide inspiration for designing macroscale metamaterials [37,38]. A polar elastic metamaterial is designed by constructing a frame similar to the lattice structure of pyrochlore crystals [39]. The auxetic behavior of rutile-structure crystals inspires a three-dimensional (3D) structure with simultaneous NPR and negative compressibility [40]. After studying the microscopic deformation characteristics of PbO crystal, a PbO-mimic lattice metamaterial with simultaneously NPR, compressibility, and thermal expansion is achieved [41]. These successes imply the feasibility of designing macroscopic metamaterials by mimicking microscopic atomic lattices. However, existing research about scaled-up NPR is limited. The design and optimization from microscale to macroscale for auxetic metamaterial remains a challenge.

In this paper, we explore the microscopic deformation mechanism of body-centered cubic (b.c.c) Ti crystal with a NPR. It is revealed that the auxetic effect is due to the rhombuses structures made up of bonds. Then a macroscale auxetic metamaterial mimicking the atomic lattice structure of Ti is designed. The mechanical properties of the auxetic metamaterial are investigated by theoretical, numerical and experimental method. The results show that the NPR mechanism of the atomic lattice keeps valid when scaled up to macroscale beam system. Moreover, the geometric parameter studies show that the NPR and normalized Young's modulus of this metamaterial can be tailored by adjusting the geometric parameters. Subsequently, an optimized structure with notably enhanced auxeticity and Young's modulus is realized based on the parametric studies.

2. The auxetic behavior of Ti crystal

To explore the microscopic mechanism for the deformation of atomic lattice crystal, density functional theory (DFT) simulation is conducted using the Vienna ab initio simulation package [42,43]. The generalized gradient approximation method of Perdewe-Burkee-Ernzerh [44] is employed to describe the electronic exchange and correlation interaction of electrons. The DFT results indicate that the atomic lattice of the Ti crystal has relatively simple crystal structures and obvious NPR, which means it may serve as a promising inspiration for the design of macroscopic auxetic metamaterials.

The atomic lattice of Ti crystal is shown in Fig. 1(a), which contains two-unit cells connecting in the [001] direction. Ti crystal is b.c.c structure (Im-3m, Oh9), with each cubic cell containing two Ti atoms located at Wyckoff coordinate 4a position. The lattice constants in the [100],

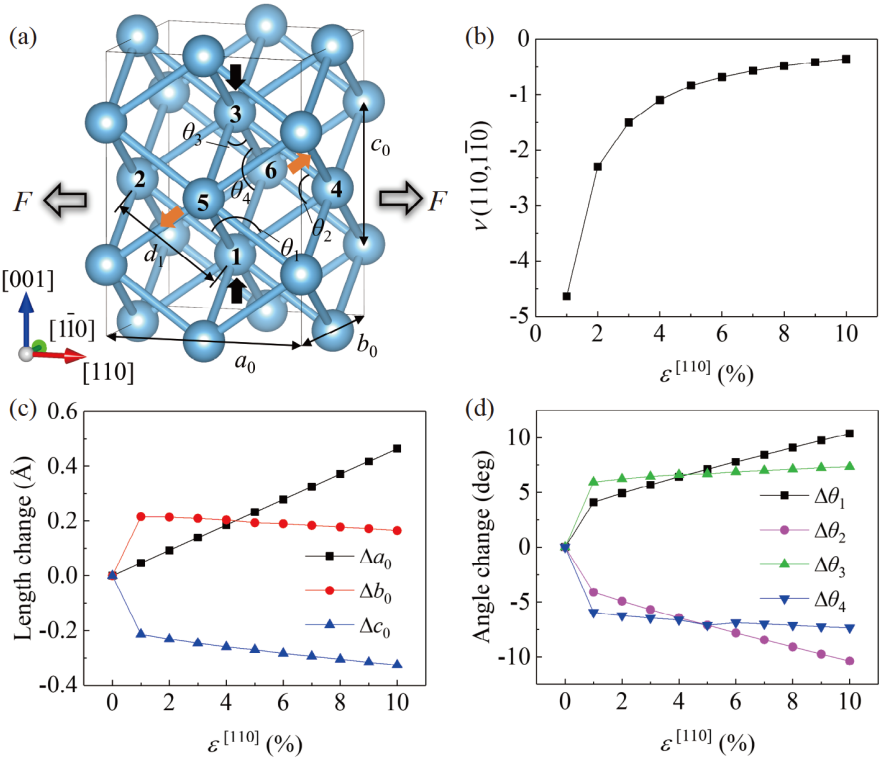

Figure 1 Atomic lattice and DFT simulation results of Ti crystal. (a) The atomic lattice of Ti crystal and its mechanism of NPR. (b) DFT prediction for Poisson's ratio $\nu(110, 1\bar{1}0)$ in terms of tensile strain $\varepsilon^{[110]}$. The changes of the (c) lengths and (d) angles with tensile strain $\varepsilon^{[110]}$.

[010], and [001] directions are a_0, b_0 and c_0, respectively. The dimensions of a unit cell in the [110], [1$\bar{1}$0], and [001] directions are denoted by a_0, b_0 and c_0, respectively. The bond angles formed by atoms 2, 1, 4 and 3, 2, 4 is denoted by θ_1. Similarly, the bond angles θ_2 (angle 123 and 143), θ_3 (angle 516 and 536) and θ_4 (angle 153 and 163) are depicted in Fig. 1(a), respectively.

The periodic crystal is stretched along the [110] direction with a strain of $\varepsilon^{[110]} = \Delta a_0/a_0$. The strain along the [1$\bar{1}$0] direction $\varepsilon^{[1\bar{1}0]} = \Delta 2c_0/2c_0$ is calculated. Then the Poisson's ratio $\nu(110, 1\bar{1}0) = \varepsilon^{[110]}/\varepsilon^{[1\bar{1}0]}$ is obtained and depicted in Fig. 1(b). The length changes and angle changes of the crystal are shown in Fig. 1(c) and (d). When the tensile strain reaches 2%, the length of a_0 and b_0 increases, and c_0 decreases, which mean that the system presents an NPR in the plane perpendicular to [001]. When the tensile strain $\varepsilon^{[110]}$ is under 10%, a_0 increases and c_0 decreases monotonically, while b_0 firstly increases obviously and decreases slightly (Fig. 1(c)). Although b_0 is slightly reduced, it is always larger than its original value when the tensile strain is under 10%. The bond angles θ_1 and θ_3 increase monotonically, while θ_2 and θ_4 decrease monotonically during the stretch, as shown in Fig. 1(d).

To explain the mechanism of NPR in the atomic lattice of Ti, we can focus on the deformation of two unit cells, as depicted in Fig. 1(a). When tensile strain is exerted in the [110] direction (as indicated by the white arrows in Fig. 1 (a)), the length of a_0 increases. The angle θ_1 increases and θ_2 decreases, which means that the rhombus consisting of atoms 1, 2, 3 and 4 (rhombus 1234) extends along the [110] direction and contracts along the [001] direction. The rhombuses on the (110, 001) boundaries undergo the same deformation. Hence, the upper atoms of these rhombuses move up, and the lower atoms move down. The atoms 1 and 3 move inwards along the [001] direction (the black arrows in Fig. 1(a)) and c_0 decreases. These displacements result in the extensions along [1$\bar{1}$0] direction of rhombus 1536 and rhombuses on the (110, 1$\bar{1}$0) boundaries. Thereby the angle θ_3 increases and θ_4 decrease. These changes cause atoms 5 and 6 to move outwards along the [1$\bar{1}$0] direction (the orange arrows in Fig. 1(a)) and the distance b_0 increases. Therefore, when stretched along the [110] direction, the unit cells expand along [1$\bar{1}$0] direction. The NPR effect of Ti crystal is attributed to the linking rhombuses in the atomic lattice.

3. Macroscopic auxetic metamaterial design and theoretical analysis

3.1 The atomic lattice-mimic design for macroscopic auxetic metamaterial

To attain the special auxetic property in macroscale, a macroscopic architected structure consisting of elastic beams is designed. Figure 2 shows the atomic lattice-mimic design for the macroscopic structure. The design starts from the microscopic crystal structure. Firstly, a proper representative unit cell of the atomic lattice should be selected to design the macroscopic metamaterial. Considering the auxetic mechanism of Ti crystal, we choose a new unit cell different to the primitive unit cell or conventional unit cell of the body-centered cube, as shown in Fig. 2(a). The newly selected unit cell helps to present and analyze the auxetic mechanism more intuitively and it can also be repeated periodically along the Cartesian axes. Secondly, the precise locations of each atom of Ti are obtained. Thirdly, to transfer the atomic lattice to an architected structure, each atom is represented as a node within the macroscopic framework. The atom positions are then mapped to the nodes of the macrostructure. Subsequently, macroscale elastic beams are used to connect these organized nodes in the similar way that atoms are connected via bonds. Lastly, to scale up the microscale lattice structure to macroscale, the length of l_2 is designed as 21.119 mm, which corresponds to the bond d_4 with the length of 2.816 Å. A macroscopic unit cell of Ti crystal-mimic structure consisting of beams is obtained, as shown in Fig. 2 (b). Noting that the NPR exists in the [100] [010] plane but along the [110] and [1$\bar{1}$0] directions, the directions of the Cartesian axes x, y, and z for the macroscopic structure are in

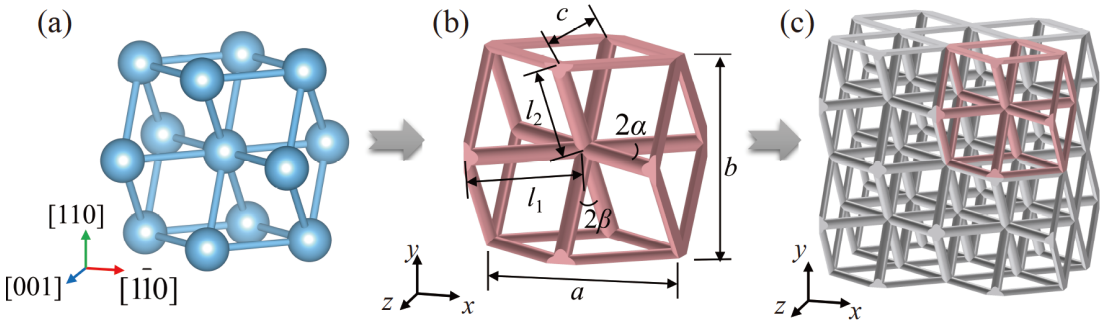

Figure 2 Atomic lattice-mimic design for the macroscopic auxetic metamaterial. (a) The new unit cell of Ti crystal; (b) the macroscopic unit cell of Ti crystal-mimic structure; (c) a macroscopic periodic lattice structure consisting of unit cells.

accordance with the directions of [1$\bar{1}$0], [110] and [001], respectively. Therefore, the macroscopic unit cell can be periodically arranged along the x, y and z directions to obtain the 3D periodic lattice structure (Fig. 2(c)).

In the macroscopic unit cell, the cross-section of the beam is assumed to be a circle with diameter d. The beams located within the boundary planes exhibit half of the thickness because they are divided by adjacent unit cells, as shown in Fig. 2(b). All the beams parallel to the xz plane are of the same length l_1, and make an angle α ($0 < \alpha < \pi/2$) with the xy plane. All the beams parallel to the yz plane are of the same length l_2, and make an angle β ($0 < \beta < \pi/2$) with the xy plane. The dimensions of the unit cell in the x, y and z directions are designated as a, b and c, respectively. Given that the beam length of l_2 has been defined as 21.119 mm, the remaining geometric dimensions are: $l_1 = l_2 = 21.119$ mm, a = c = 34.487 mm, b = 24.386 mm, $\alpha = \beta = 0.6155$.

3.2 Theoretical analysis of macroscopic mechanical properties

To obtain the analytical models of the Poisson's ratio and normalized Young's modulus, a theoretical model is built for the unit cell of the atomic lattice-mimic structure, as demonstrated in Fig. 3. As the macroscopic auxetic metamaterial is constructed with slender beam, it is assumed that the beams are Euler-Bernoulli beams by neglecting the shear deformation. In addition, it is supposed that the material is in the linear elastic range and in small deformations, so the geometric nonlinearity is not considered in the theoretical analysis.

Consider that a uniformly distributed stress σ_2 is applied to the unit cell in the y direction. Figure 3(a) illustrates the forces exerted on the boundaries of the unit cell. In the unit cell there is a geometrical relationship $l_1\sin\alpha = l_2\sin\beta$. The beams located within the boundaries (the green beams in Fig. 3(a)) only show half of the thickness. Based on periodicity and symmetry, the xz and yz boundaries remain planar and no rotations occur. Thus, the beams in the xz boundaries have identical forces F_2 along the y direction at the ends, and deform only in the xz plane. So the beams parallel to the yz plane are subjected to forces along the y and z directions, and the beams parallel to the xz plane are not subjected to forces in the x direction. It can be found that $\sigma_2 = F_2 l_1^2 \sin\alpha\cos\alpha$ and $S_3 + T_3 = 0$. The deformation of the periodic structure can be obtained by analyzing the forces of beams OA and OB. The forces and moments acting on the end of the beams are sketched in Fig. 3(b) and (c), where the beams in grey are structures symmetric about the xy plane within the unit cell. The beam OB is clamped at the end node O, and at the end B undergoes a force F_2 along the y direction, a force S_3 along the z direction and a bending moment M_1 about the x direction. The beam OA is clamped at the end node O, and at the end A undergoes a force T_3 along the z direction as well as a bending moment M_2 about the y direction.

As there is no rotation at end B, the moment acting on end B is

$$M_1 = -\frac{1}{2}l_2F_2\sin\beta + \frac{1}{2}l_2S_3\cos\beta. \tag{1}$$

Then the relative displacements of point B to point O in the y and z directions can be expressed respectively by

$$\delta_{B2} = \frac{1}{K_{f2}}(F_2\sin\beta - S_3\cos\beta)\sin\beta + \frac{1}{K_{s2}}(F_2\cos\beta + S_3\sin\beta)\cos\beta, \tag{2}$$

$$\delta_{B3} = \frac{1}{K_{f2}}(-F_2\sin\beta + S_3\cos\beta)\cos\beta + \frac{1}{K_{s2}}(F_2\cos\beta + S_3\sin\beta)\sin\beta, \tag{3}$$

with

$$K_{f2} = \frac{3\pi d^4 E_s}{16 l_2^3},\quad K_{s2} = \frac{\pi d^2 E_s}{4 l_2}, \tag{4}$$

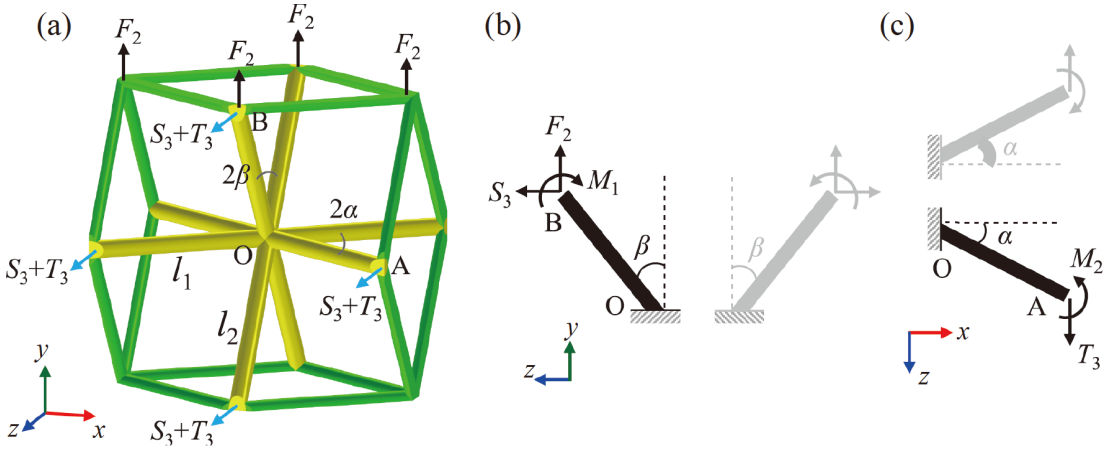

Figure 3 Theoretical model of the macroscopic unit cell. (a) Forces acting on the boundaries of the unit cell; (b) forces and moments acting on the B end of beam OB; (c) forces and moments acting on the A end of beam OA.

where E_s is the Young's modulus of the parent material.

As there is no rotation at end A, we have

$$M_2 = \frac{1}{2} l_1 T_3 \cos\alpha. \tag{5}$$

Then the relative displacements of point A to point O in the y and z directions can be calculated respectively by

$$\delta_{A1} = -\frac{1}{K_{f1}} T_3 \cos\alpha \sin\alpha + \frac{1}{K_{s1}} T_3 \sin\alpha \cos\alpha, \tag{6}$$

$$\delta_{A3} = \frac{1}{K_{f1}} T_3 \cos\alpha \cos\alpha + \frac{1}{K_{s1}} T_3 \sin\alpha \sin\alpha, \tag{7}$$

with

$$K_{f1} = \frac{3\pi d^4 E_s}{16 l_1^3}, \quad K_{s1} = \frac{\pi d^2 E_s}{4 l_1}. \tag{8}$$

Considering the periodicity, end A and end B always lie in a plane parallel to the xy plane, that is, point A and point B have the same displacement along the z direction, which can be expressed as

$$\delta_{A3} = \delta_{B3}. \tag{9}$$

By using Eqs. (4) and (7) as well as the relation $S_3 + T_3 = 0$, it can be obtained that

$$S_3 = kF_2, \quad T_3 = -kF_2, \tag{10}$$

where k is defined by

$$k = \frac{\left(\frac{1}{K_{f2}} - \frac{1}{K_{s2}}\right) \sin\beta \cos\beta}{\frac{\cos^2\alpha}{K_{f1}} + \frac{\sin^2\alpha}{K_{s1}} + \frac{\cos^2\beta}{K_{f2}} + \frac{\sin^2\beta}{K_{s2}}}. \tag{11}$$

Then the strains of the unit cell can be derived as

$$\varepsilon_1 = \frac{2\delta_{A1}}{a} = -\frac{F_2 k \sin\alpha (K_{f1} - K_{s1})}{l_1 K_{f1} K_{s1}}, \tag{12}$$

$$\varepsilon_2 = \frac{2\delta_{B2}}{b} = \frac{F_2 \left[(K_{f2} - K_{s2}) \cos^2\beta + k \sin\beta (K_{f2} - K_{s2}) \cos\beta + K_{s2}\right]}{l_2 K_{f2} K_{s2} \cos\beta}, \tag{13}$$

$$\varepsilon_3 = \frac{2\delta_{A3}}{c} = \frac{F_2 k \left[(K_{f1} - K_{s1}) \cos^2\alpha - K_{f1}\right]}{l_1 K_{f1} K_{s1} \sin\alpha}. \tag{14}$$

Accordingly, the Poisson's ratios along the x and z directions are respectively

$$\nu_{yx} = -\frac{\varepsilon_1}{\varepsilon_2} = \frac{l_2 k K_{f2} K_{s2} (K_{f1} - K_{s1}) \sin\alpha \cos\beta}{l_1 K_{f1} K_{s1} \left[K_{s2} + (K_{f2} - K_{s2})(\cos^2\beta + k \sin\beta \cos\beta)\right]}, \tag{15}$$

$$\nu_{yz} = -\frac{\varepsilon_3}{\varepsilon_2} = -\frac{l_2 k K_{f2} K_{s2} \cos\beta \left[(K_{f1} - K_{s1}) \cos^2\alpha - K_{f1}\right]}{l_1 K_{f1} K_{s1} \sin\alpha \left[K_{s2} + (K_{f2} - K_{s2})(\cos^2\beta + k \sin\beta \cos\beta)\right]}. \tag{16}$$

The effective Young's modulus E_y in the y direction is

$$E_y = \frac{\sigma_2}{\varepsilon_2} = \frac{l_2 K_{f2} K_{s2} \cos\beta}{l_1^2 \sin\alpha \cos\alpha \left[K_{s2} + (K_{f2} - K_{s2})(\cos^2\beta + k \sin\beta \cos\beta)\right]}. \tag{17}$$

Then the normalized Young's modulus of the unit cell can be calculated as E_y/E_s.

4. Finite-element simulations and experimental tests

4.1 Finite-element method

To analyze the deformation mode and mechanical properties of the designed metamaterial, finite-element simulation model is introduced and investigated using the finite-element simulation software. The unit cells maintain the same geometric dimensions as detailed in Sect. 3.1. A periodic lattice structure with 2×6×2 unit cells is used for finite-element simulation, as shown in Fig. 4(a). The size of the lattice structure in the x, y and z directions are 71.974 mm, 231.92 mm and 51.772 mm, respectively. Two solid blocks are embedded to facilitate the loading process and ease the calculation of results.

Free tetrahedral solid elements are used in the finite-element model. Mesh convergence analysis indicates that with a minimum mesh size of 0.997 mm, the model is sufficient to produce accurate outcomes, including the effective Poisson's ratio and the effective Young's modulus. To simulate the structural deformation as much as possible and compare with the subsequent experimental results, geometric nonlinearity is considered in the stationary analysis. In the simulation, a displacement is imposed on the upper solid block along the y direction (equal to up to 14% of the longitudinal length of the lattice structure), while the lower solid block is fixed.

The sweep of loading stain is assigned in the analysis to gain the deformation process. When the analysis is complete, a volume integral is employed on the solid blocks to ascertain the loading response, thereby enabling the stress and effective Young's modulus to be derived. To circumvent the influence of boundary effects, longitudinal and transverse strains of the 2×2×2 unit cells in the central portion of the model (the red dotted rectangle in Fig. 4(a)) are obtained to calculate the effective Poisson's ratio of the structure.

4.2 Experimental setup

In order to validate the auxeticity of the designed metamaterial, quasi-static uniaxial tensile tests are conducted. Geometry configuration of the specimens is the same as the finite-element simulation model. Utilising nylon as the parent material, the metamaterial specimens are produced

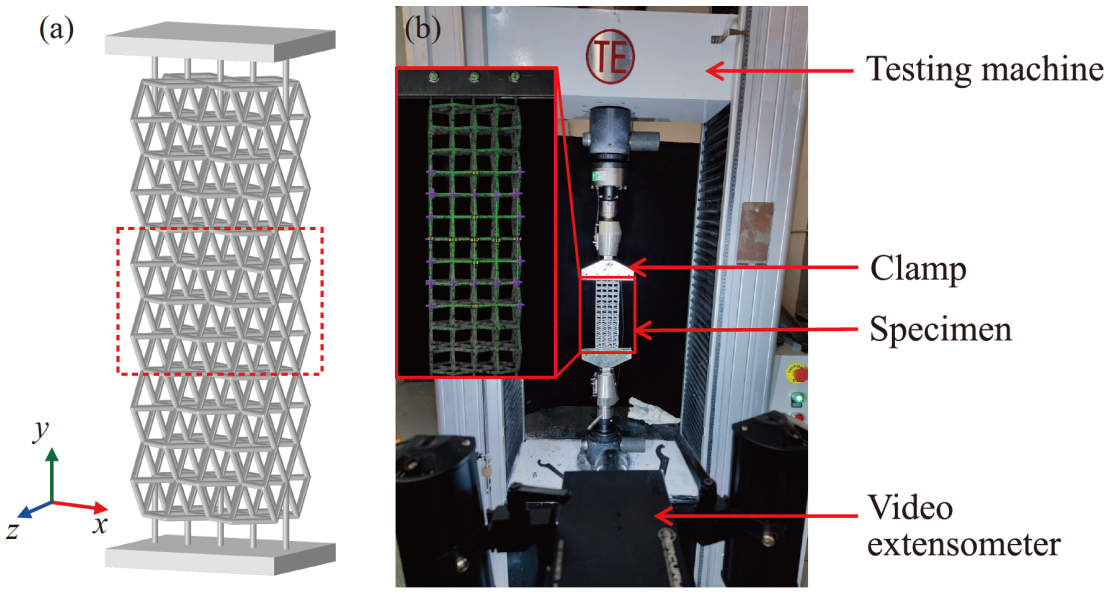

Figure 4 (a) Finite-element simulation model and (b) experimental set up for the quasi-static uniaxial tensile tests.

via the selective laser sintering method. Uniaxial tensile tests are firstly operated on the dog-bone shaped specimens in order to obtain the mechanical properties of the parent material, with a tensile rate set at 2 mm/min. The true stress-strain curves are derived, revealing the Young's modulus E_s of the parent material to be 616 MPa.

Uniaxial tensile tests are performed on two identical metamaterial specimens to ensure the repeatability. The experimental set up for the quasi-static uniaxial tensile tests is illustrated in Fig. 4(b). The quasi-static uniaxial tensile tests are conducted on a 200 kN Instron testing machine. Specimens are held in between the top and bottom clamps. The bottom clamp is fixed, while the top clamp moves up at a displacement rate of 5 mm/min. The load-displacement response was recorded by the testing machine with a sampling rate of 10 times/s. And then the loading strain and stress can be derived. During the tensile process, the dimensions and strains are recorded using a digital image correlation system with a video extensometer. Similar to the finite-element simulations, longitudinal and transverse strains of the 2×2×2 unit cells in the central portion of the specimen are obtained to calculate the Poisson's ratio.

5. Results and discussions

5.1 Comparison between theoretical, numerical and experimental results

This section presents an investigation into the Poisson's ratio and the normalized Young's modulus of the atomic lattice-mimic metamaterial. In addition, the results of theoretical analysis, finite-element analysis (FEA) and experiments are compared and discussed, which validates the auxeticity of the designed atomic lattice-mimic structure.

The deformation patterns of the atomic lattice-mimic structure at 10% loading strain are shown in Fig. 5. The deformation patterns obtained from FEA (Fig. 5(a)) and the experiment (Fig. 5(b)) are similar. The shape defined by the black lines in Fig. 5(a) corresponds to the initial configuration of the structure. The lateral deformation demonstrates that the structure expands transversely when subjected to longitudinal tension along the y direction, which indicates its auxetic characteristic. The deformation of a unit cell is shown in Fig. 5(c). The grey configuration is the undeformed unit cell, and the green configuration is the deformed unit cell.

When stretched along the y direction (the white arrows in Fig. 5(c)), the rhombuses BKFL and DJHM which lie in the xz boundaries move outward along the y direction. These movements cause the deformation of the beams in the yz plane. Rhombuses CMGL and AJEK extend along the y direction and contract along the z direction. Under the combined action of rhombuses AJEK and beams OA and OE, the nodes A and E move close to each other along the z direction and move along the x direction (the purple arrows). Similarly, the nodes C and G move close to each other along the z direction and move along the negative direction of x axis (the purple arrows). Thus the rhombus AJEK moves along the x direction, and the rhombus CMGL moves along the negative direction of x axis. As a result, the nodes LMJK move away from each other in the xy plane (the yellow arrows). The extension of rhombus BKFL along the x direction causes the contraction of itself in the z direction. So the nodes B and F move close to each other in the z direction (the blue arrows). Due to the symmetry of the unit cell, the nodes D and B also move close to each other (the blue

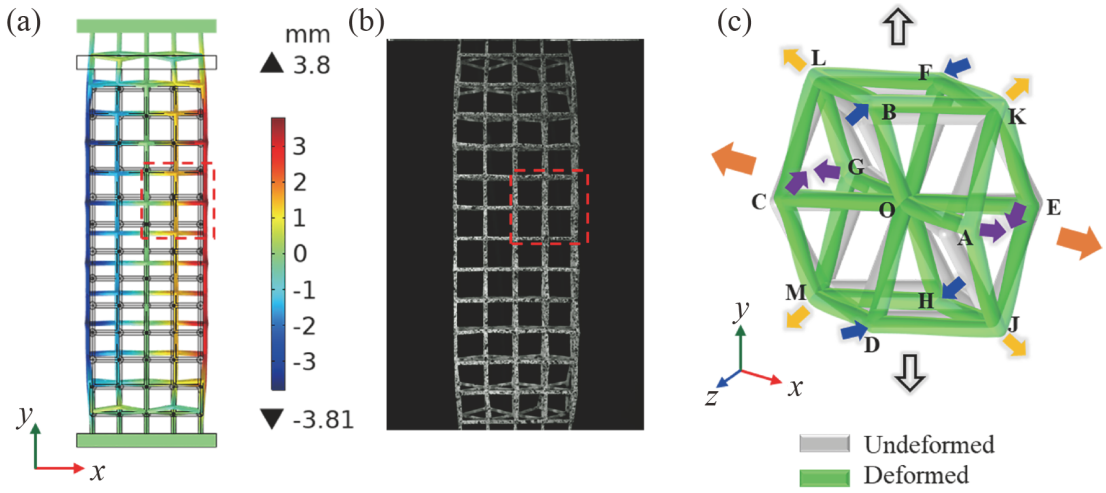

Figure 5 Deformation patterns of the atomic lattice-mimic structure at 10% loading strain. (a) Displacement in the x direction obtained from FEA; (b) the deformation of the specimen obtained from the experiment; (c) deformation analysis of a unit cell. The shape defined by the black lines in (a) corresponds to the initial configuration of the structure. The red dashed lines in (a) and (b) show the corresponding unit cell in (c).

arrows). Therefore, when the unit cell is stretch along the y direction, it expands along the x direction (the orange arrows), which means the structure is auxetic. The NPR effect of the macroscopic Ti-mimic structure is attributed to the linking rhombuses in the unit cell.

The deformation mechanism of the macroscopic Ti-mimic structure is similar to that of the microscopic Ti crystal. The crystal lattice deformation arises from the alterations in the bond lengths and angles, predominantly due to the changes of the interaction force between atoms [45,46]. Furthermore, the deformation of the atomic lattice may be affected by the interactions between or within atoms, which are complex [47-50]. On the other hand, the deformation of the designed macroscopic Ti-mimic structure is mainly attributable to the axial tension, compression, bending and torsion of the elastic beams, which alter the position of the nodes.

As shown in Fig. 6, comparing the theoretical results, FEA results and experimental results, the curves are in close agreement with each other. Figure 6(a) and (b) indicates the auxeticity of the atomic lattice-mimic structure. The Poisson's ratio obtained from theoretical analysis, FEA and experiments are −0.877, −0.823 and −0.905, respectively. The design approach for the auxetic metamaterial inspired by the crystal structure of Ti is proved to be feasible by the consistency between these results.

To evaluate the effective Young's modulus of the structure, the normalized Young's modulus E_y/E_s is defined as the ratio of effective Young's modulus E_y to Young's modulus of parent material E_s. Figure 6(c) and (d) shows the comparisons of the stress-loading strain and E_y/E_s-loading strain curves from the theoretical, FEA and experimental results. The normalized Young's modulus E_y/E_s obtained from theoretical analysis, FEA and experiments are 2.270×10^{-3}, 2.256×10^{-3}, 2.648×10^{-3}, respectively.

The slight differences in the theoretical, FEA and experimental results may be due to the simplification of the beam theory, the boundary conditions and the nonlinearity of material and geometry. Moreover, the experimental result may be influenced by the parameters of the 3D printing process of the specimen [51,52]. The differences among different methods are acceptable, and the theoretical results can describe the mechanical properties of the metamaterials accurately. Hence, the characteristics of the metamaterial analyzed by the theoretical method are reliable as well as efficient.

It is worth noting that the Poisson's ratio changes little as longitudinal strain increases, as shown in Fig. 6(b). In the finite-element simulation, when the loading strain is less than 10%, the Poisson's ratio of the auxetic metamaterial varies within 6.25%. In contrast, for other auxetic materials, the NPR weakens up to 50% at a small loading strain of 5% [53]. It can be posited that the Poisson's ratio v_{yx} of the proposed auxetic metamaterial is strain-independent when the loading strain is lower than 10%. This overcomes the problem of strain-dependent auxeticity in most auxetic metamaterials and can broaden the application of auxetic metamaterials.

5.2 Geometric parameter investigation

In this section, the relationships between the geometric parameters and the mechanical properties of the metamaterial are discussed. The Poisson's ratio v_{xy} and normalized Young's modulus E_y/E_s of the structure are analyzed using the theoretical model introduced above.

Firstly, in the theoretical model, it is set that $l_1 = l_2 = 21.119$ mm and $\alpha = \beta$. The effects of angle $\alpha(\beta)$ and diameter d are demonstrated in Fig. 7(a) and (b). As α and β increases

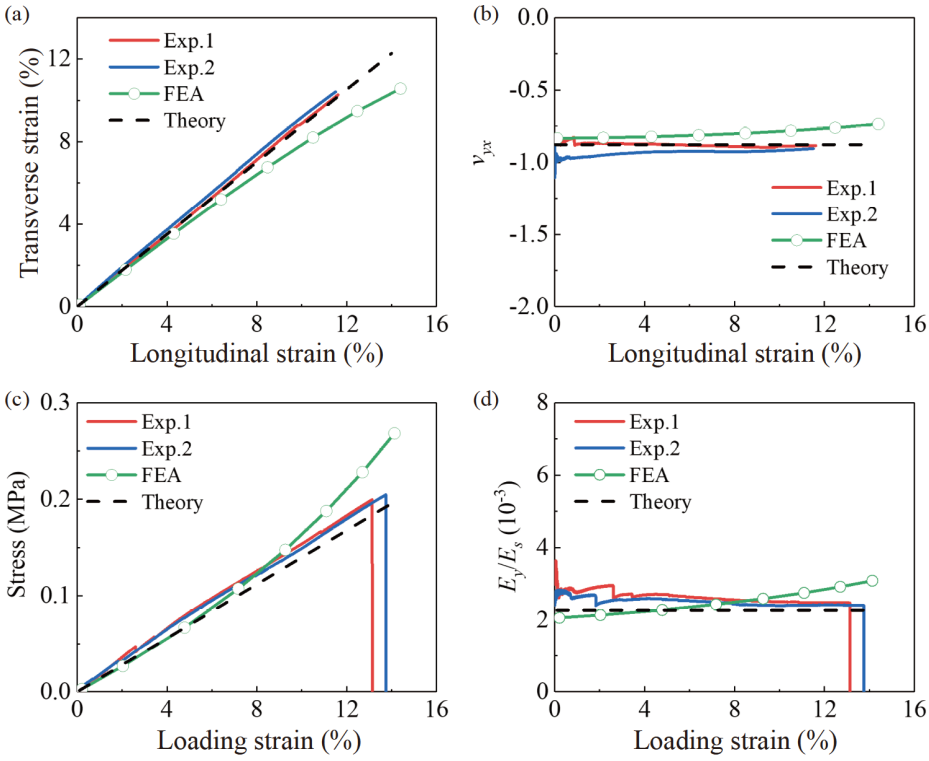

Figure 6 Comparisons of (a) transverse strain-longitudinal strain curves, (b) effective Poisson's ratio v_{yx}-longitudinal strain curves, (c) stress-loading strain curves and (d) normalized Young's modulus E_y/E_s-loading strain curves of the theoretical, FEA and experimental results of the atomic lattice-mimic metamaterial.

from 0 to $\pi/2$, v_{yx} first decreases and then increases. The Poisson's ratio v_{yx} reaches maximum values when α and β is equal to $\pi/4$. When α and β are fixed, v_{yx} decreases with increasing d. Besides, normalized Young's modulus E_y/E_s increases when d increases or $\alpha(\beta)$ decreases.

To obtain a structure with larger NPR and normalized Young's modulus, it is set that $l_1 = 21.119$ mm, $d = 5.2$ mm and $\alpha \neq \beta$, and then the effects of angle α and β are shown in Fig. 7(c) and (d). The Poisson's ratio v_{yx} decreases with increasing α. With fixed α, v_{yx} first decreases and then increases when β increases. The normalized Young's modulus E_y/E_s decreases with increasing β, and it first decreases and then increases with increasing α. Through parameter design, the Poisson's ratio v_{yx} can be tailored from -6 to 0, and the normalized Young's modulus E_y/E_s can be tailored from 0 to 0.8.

The parametric studies reveal that the Poisson's ratio and normalized Young's modulus of the auxetic metamaterial are tailorable through adjusting the geometric parameters. The mechanical properties of metamaterials can be designed according to different application requirements, which may broaden the applications of auxetic metamaterials.

5.3 Optimization design

To obtain an auxetic structure with larger NPR and normalized Young's modulus, an optimized structure is proposedbased on the parametric studies. The unit cell of the optimized structure is shown in Fig. 8(a). The geometric parameters of the unit cell are: $d = 5.2$ mm, $\alpha = 1.2566$, $\beta = 0.5921$, and l_1 keeps the same value as the original atomic lattice-mimic structure, which is 21.119 mm.

As the change of the size of the unit cell and the limitation of the size of the clamp, a periodic lattice structure with 2×5×1 unit cells is used for the numerical and experimental studies. Finite-element simulations and quasi-static uniaxial tensile tests are conducted on the optimized structure. The finite-element simulation model is shown in Fig. 8(b). The lateral deformation of the lattice structure at a loading stain of 8% is illustrated in Fig. 8(b), which reveals that the optimized structure has apparent auxeticity.

The mechanical properties of the optimized metamaterial obtained from experiments and FEA are shown in Fig. 8(d) and (e). The Poisson's ratio v_{yx} obtained from the FEA and experiment are -1.621 and -1.751, respectively. And the normalized Young's modulus E_y/E_s are 0.071 and 0.067, respectively. It is observed that the effective Poisson's ratio v_{yx} -longitudinal strain curves obtained from FEA and experiment are in good agreement with each other. The curve of normalized Young's modulus E_y/E_s obtained from experiment vibrates before 1.3% loading strain, which is mainly due to the relative slip between the clamp and the specimen.

Comparisons of the geometric parameters and mechanical properties of the original atomic lattice-mimic structure and the optimized structure are demonstrated in Table 1. After

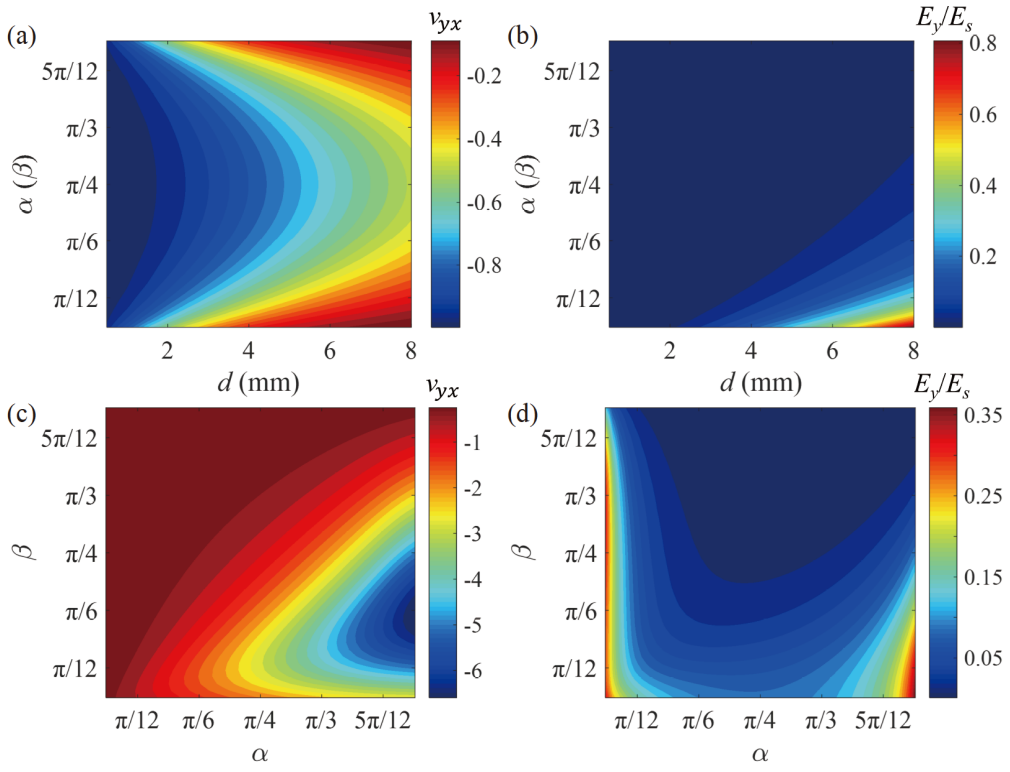

Figure 7 Dependences of Poisson's ratio v_{yx} and normalized Young's modulus E_y/E_s on the geometric parameters. In (a) and (b) it is set that $\alpha = \beta$, while in (c) and (d) it is set that $\alpha \neq \beta$ and $d = 5.2$ mm.

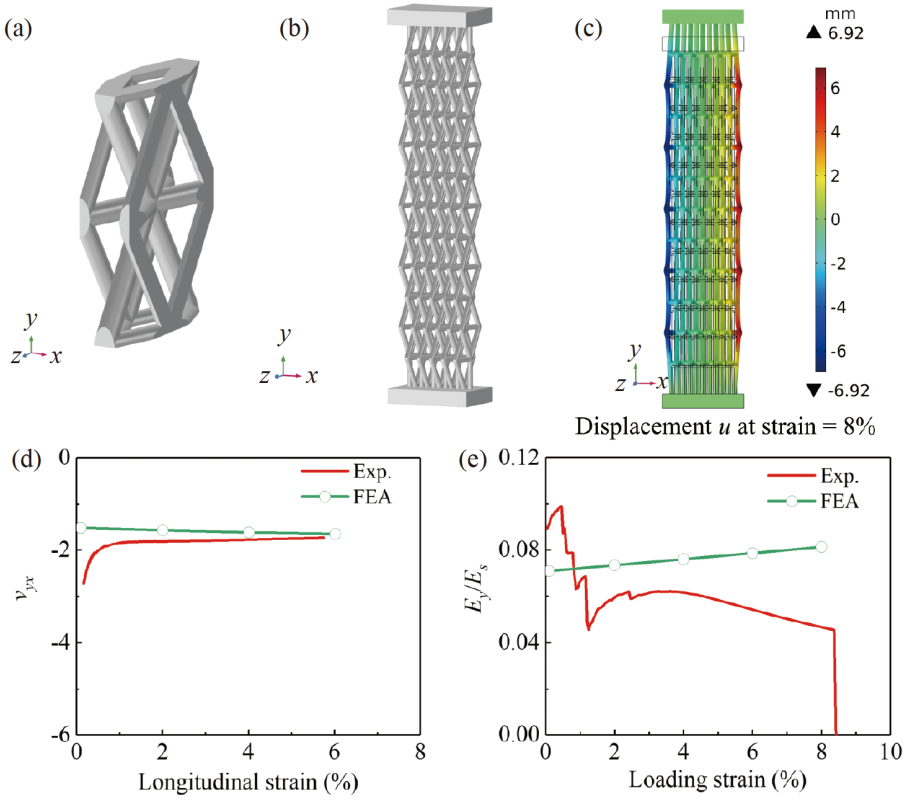

Figure 8 Schematics of the optimized structure: (a) unit cell, (b) finite-element simulation model and (c) the lateral deformation of the lattice structure at 8% loading strain. Mechanical properties of the optimized metamaterial: (d) effective Poisson's ratio v_{yx} and (e) normalized Young's modulus E_y/E_s.

Table 1 Comparisons of geometric parameters and mechanical properties of the original atomic lattice-mimic structure and the optimized structure

	Original structure	Optimized structure
l_1 (mm)	21.119	21.119
l_2 (mm)	21.119	35.988
α	0.6155	1.2566
β	0.6155	0.5921
d (mm)	3.0	5.2
ν_{xy}	−0.905	−1.751
E_y/E_s	2.648×10^{-3}	0.067

the optimization, the effective Poisson's ratio can reach −1.751, with nearly 2 times enhancement of auxeticity compared to the origin structure. The normalized Young's modulus is enlarged from 2.648×10^{-3} to 0.067, with an improvement of 25 times. The auxeticity and the stiffness of the metamaterial are both significantly improved through optimization design, which may make this metamaterial have greater application prospects.

6. Conclusion

In conclusion, the mechanism of auxeticity in microscale Ti crystal is investigated through DFT simulation. It is found that the auxetic effect of Ti crystal is attributed to the rhombuses in the atomic lattice. Then a macroscopic auxetic metamaterial is designed by mimicking the atomic lattice of Ti crystal.

The auxeticity of the macroscopic metamaterial is validated by theoretical, numerical and experimental methods. Besides, the Young's modulus of the metamaterial is investigated.

Furthermore, the geometric parameter investigation shows that the NPR and normalized Young's modulus of the metamaterial can be tailored by adjusting the geometric parameters. The Poisson's ratio of the metamaterial can be tailored from −6 to 0, and the normalized Young's modulus can be tailored from 0 to 0.8.

Through the optimization design, an optimized metamaterial is achieved, displaying 2 times increase in auxeticity and 25 times increase in in normalized Young's modulus, compared to the initial architectures.

This work provides inspirations of auxetic metamaterial design, and lays a foundation for the application of auxetic metamaterials.

Conflict of interest *On behalf of all authors, the corresponding author states that there is no conflict of interest.*

Author contributions ***Jiahui Zhou:*** *Conceptualization, Methodology, Software, Data Curation, Investigation, Writing – original draft.* ***Yuhang Liu, Zunyi Deng****, and* ***Yingzhuo Lun:*** *Conceptualization, Methodology, Data Curation.* ***Xingang Jiang****,* ***Zhong Zhang*** *and* ***Hongshuai Lei:*** *Resources, Methodology.* ***Wenhao Xiao*** *and* ***Li Meng:*** *Investigation.* ***Bo Yu*** *and* ***Gang Tang:*** *Methodology.* ***Zewei Hou:*** *Project administration, Funding acquisition, Writing – review & editing.* ***Jiawang Hong:*** *Supervision, Funding acquisition, Writing – review & editing.*

Acknowledgements *This work was supported by the National Key R&D Program of China (Grant No. 2021YFA1400300), the National Natural Science Foundation of China (Grant Nos. 12172047, 12372177, and 12102007), Beijing Natural Science Foundation (Grant Nos. 1244057 and Z190011), and Beijing Institute of Technology Research Fund Program for Young Scholars. Calculations were performed using resources of the Supercomputer Centre in Chongqing.*

1 J. Fan, L. Zhang, S. Wei, Z. Zhang, S. K. Choi, B. Song, and Y. Shi, A review of additive manufacturing of metamaterials and developing trends, Mater. Today **50**, 303 (2021).
2 Y. Gao, and L. Wang, An active tunable piezoelectric metamaterial beam for broadband vibration suppression by optimization, Acta Mech. Sin. **40**, 523235 (2024).
3 Y. Miyazawa, H. Yasuda, and J. Yang, Design of compliant mechanisms for origami metamaterials, Acta Mech. Sin. **39**, 723169 (2023).
4 Y. Xiang, J. Tian, K. Tang, X. Wang, and Z. Zhong, Morphological design and tunable mechanical properties of 3D spinodal membrane structures: Adaptive coarse-grained modelling, Acta Mech. Sin. **40**, 423655 (2024).
5 X. L. Peng, and S. Bargmann, Tunable auxeticity and isotropic negative thermal expansion in three-dimensional lattice structures of cubic symmetry, Extreme Mech. Lett. **43**, 101201 (2021).
6 S. Shukla, and B. K. Behera, Auxetic fibrous structures and their composites: A review, Compos. Struct. **290**, 115530 (2022).
7 X. Cai, T. Yang, W. Qin, and Z. Xie, A quasi-zero stiffness energy harvesting isolator with triple negative stiffness, Acta Mech. Sin. **40**, 523531 (2024).
8 Z. Li, Z. Luo, L. C. Zhang, and C. H. Wang, Topological design of pentamode lattice metamaterials using a ground structure method, Mater. Des. **202**, 109523 (2021).
9 Y. Wang, H. Zhao, H. Yang, J. Liu, D. Yu, and J. Wen, Topological design of lattice materials with application to underwater sound insulation, Mech. Syst. Signal Process. **171**, 108911 (2022).
10 J. Ju, and J. D. Summers, Compliant hexagonal periodic lattice structures having both high shear strength and high shear strain, Mater. Des. **32**, 512 (2011).
11 S. Yang, V. B. Chalivendra, and Y. K. Kim, Fracture and impact characterization of novel auxetic Kevlar®/Epoxy laminated composites, Compos. Struct. **168**, 120 (2017).
12 D. Photiou, N. Prastiti, E. Sarris, and G. Constantinides, On the conical indentation response of elastic auxetic materials: Effects of Poisson's ratio, contact friction and cone angle, Int. J. Solids Struct. **81**, 33 (2016).
13 H. Ding, N. Huang, N. Muhammad, C. Xu, and L. Tong, Negative Poisson's ratio locally resonant seismic metamaterials vibration isolation barrier, Acta Mech. Sin. **40**, 523370 (2024).
14 G. Imbalzano, S. Linforth, T. D. Ngo, P. V. S. Lee, and P. Tran, Blast resistance of auxetic and honeycomb sandwich panels: Comparisons and parametric designs, Compos. Struct. **183**, 242 (2018).
15 A. Alderson, K. L. Alderson, G. Chirima, N. Ravirala, and K. M. Zied, The in-plane linear elastic constants and out-of-plane bending of 3-coordinated ligament and cylinder-ligament honeycombs, Compos. Sci. Tech. **70**, 1034 (2010).
16 Z. Wang, C. Luan, G. Liao, J. Liu, X. Yao, and J. Fu, Progress in auxetic mechanical metamaterials: structures, characteristics, manufacturing methods, and applications, Adv. Eng. Mater. **22**, 2000312 (2020).
17 W. Jiang, X. Ren, S. L. Wang, X. G. Zhang, X. Y. Zhang, C. Luo, Y. M. Xie, F. Scarpa, A. Alderson, and K. E. Evans, Manufacturing, characteristics and applications of auxetic foams: A state-of-the-art review, Compos. Part B-Eng. **235**, 109733 (2022).
18 V. A. Lvov, F. S. Senatov, A. A. Veveris, V. A. Skrybykina, and A. Díaz Lantada, Auxetic metamaterials for biomedical devices: Current situation, main challenges, and research trends, Materials **15**, 1439 (2022).
19 J. Shen, K. Liu, Q. Zeng, J. Ge, Z. Dong, and J. Liang, Design and mechanical property studies of 3D re-entrant lattice auxetic structure,

Aerosp. Sci. Tech. **118**, 106998 (2021).
20 W. Z. Jiang, X. C. Teng, X. H. Ni, X. G. Zhang, X. Cheng, W. Jiang, D. Han, Y. Zhang, and X. Ren, An improved re-entrant honeycomb with programmable densification and multistage energy-absorbing performance, Eng. Struct. **301**, 117318 (2024).
21 J. N. Grima, and K. E. Evans, Auxetic behavior from rotating squares, J. Mater. Sci. Lett. **19**, 1563 (2000).
22 J. N. Grima, P. Farrugia, R. Gatt, and D. Attard, On the auxetic properties of rotating rhombi and parallelograms: A preliminary investigation, Phys. Status Solidi (b) **245**, 521 (2008).
23 Y. Chen, W. Ye, R. Xu, Y. Sun, J. Feng, and P. Sareh, A programmable auxetic metamaterial with tunable crystal symmetry, Int. J. Mech. Sci. **249**, 108249 (2023).
24 L. Zhang, H. Du, and W. Yu, Constitutive modeling of chiral mechanical metastructures, Acta Mech. Sin. **39**, 422342 (2023).
25 X. G. Zhang, X. Ren, W. Jiang, X. Y. Zhang, C. Luo, Y. Zhang, and Y. M. Xie, A novel auxetic chiral lattice composite: Experimental and numerical study, Compos. Struct. **282**, 115043 (2022).
26 T. Li, and Y. Li, Mechanical behaviors of three-dimensional chiral mechanical metamaterials, Compos. Part B-Eng. **270**, 111141 (2024).
27 X. Ren, R. Das, P. Tran, T. D. Ngo, and Y. M. Xie, Auxetic metamaterials and structures: A review, Smart Mater. Struct. **27**, 023001 (2018).
28 A. Sorrentino, D. Castagnetti, L. Mizzi, and A. Spaggiari, Bio-inspired auxetic mechanical metamaterials evolved from rotating squares unit, Mech. Mater. **173**, 104421 (2022).
29 F. Jiang, S. Yang, Y. Zhang, C. Qi, and S. Chen, Fabrication and crushing response of graded re-entrant circular auxetic honeycomb, Int. J. Mech. Sci. **242**, 107999 (2023).
30 F. Li, Q. Zhang, Z. Wang, and D. Zhu, A new three-dimensional re-entrant negative Poisson's ratio metamaterial with tunable stiffness, Eng. Struct. **306**, 117793 (2024).
31 R. Peng, Y. Ma, Q. Wu, B. Huang, and Y. Dai, Two-dimensional materials with intrinsic auxeticity: Progress and perspectives, Nanoscale **11**, 11413 (2019).
32 B. Wang, Q. Wu, Y. Zhang, L. Ma, and J. Wang, Auxetic B_4N monolayer: A promising 2D material with in-plane negative Poisson's ratio and large anisotropic mechanics, ACS Appl. Mater. Interfaces **11**, 33231 (2019).
33 Y. Song, N. Shi, S. Deng, X. Xing, and J. Chen, Negative thermal expansion in magnetic materials, Prog. Mater. Sci. **121**, 100835 (2021).
34 Z. Liu, Z. Wang, D. Sun, and X. Xing, Intrinsic volumetric negative thermal expansion in the "rigid" calcium squarate, Chem. Commun. **57**, 9382 (2021).
35 S. Trolier-McKinstry, S. Zhang, A. J. Bell, and X. Tan, High-performance piezoelectric crystals, ceramics, and films, Annu. Rev. Mater. Res. **48**, 191 (2018).
36 C. Qiu, B. Wang, N. Zhang, S. Zhang, J. Liu, D. Walker, Y. Wang, H. Tian, T. R. Shrout, Z. Xu, L. Q. Chen, and F. Li, Transparent ferroelectric crystals with ultrahigh piezoelectricity, Nature **577**, 350 (2020).
37 M. S. Pham, C. Liu, I. Todd, and J. Lertthanasarn, Damage-tolerant architected materials inspired by crystal microstructure, Nature **565**, 305 (2019).
38 J. N. Grima-Cornish, D. Attard, L. Vella-Żarb, J. N. Grima, and K. E. Evans, Boron arsenate scaled-up: An enhanced nano-mimicking mechanical metamaterial, Phys. Status Solidi (b) **259**, 2200368 (2022).
39 O. R. Bilal, R. Süsstrunk, C. Daraio, and S. D. Huber, Intrinsically polar elastic metamaterials, Adv. Mater. **29**, 1700540 (2017).
40 Y. Yao, Y. Ni, and L. H. He, Rutile-mimic 3D metamaterials with simultaneously negative Poisson's ratio and negative compressibility, Mater. Des. **200**, 109440 (2021).
41 Y. Yao, L. H. He, J. H. Jin, and J. Ding, A novel design of mechanical metamaterial incorporating multiple negative indexes, Mater. Res. Express **10**, 055801 (2023).
42 G. Kresse, and J. Furthmüller, Efficient iterative schemes for *ab initio* total-energy calculations using a plane-wave basis set, Phys. Rev. B **54**, 11169 (1996).
43 G. Kresse, and J. Furthmüller, Efficiency of ab-initio total energy calculations for metals and semiconductors using a plane-wave basis set, Comput. Mater. Sci. **6**, 15 (1996).
44 J. P. Perdew, K. Burke, and M. Ernzerhof, Generalized gradient approximation made simple, Phys. Rev. Lett. **77**, 3865 (1996).
45 T. C. Lim, Kinematical studies on rotation-based semi-auxetics, J. Mater. Sci. **42**, 7690 (2007).
46 P. Lv, G. Tang, C. Yang, J. Deng, Y. Liu, X. Wang, X. Wang, and J. Hong, Half-metallicity in two-dimensional Co_2Se_3 monolayer with superior mechanical flexibility, 2D Mater. **5**, 045026 (2018).
47 E. Leader, and C. Lorcé, The angular momentum controversy: What's it all about and does it matter? Phys. Rep. **541**, 163 (2014).
48 B. Li, X. Xuan, Y. Yin, J. Zhou, Z. Zhang, M. Yi, and W. Guo, Asymmetric bias-tunable surface adhesion of semiconductor nano-films, Acta Mech. Sin. **39**, 122484 (2023).
49 C. Fan, K. Liu, Y. Wang, L. Zhang, and L. Sun, Nano-indentation and nano-scratch of flexible intraocular lens material at the molecular scale, Acta Mech. Sin. **39**, 122331 (2023).
50 J. M. Goff, C. Sievers, M. A. Wood, and A. P. Thompson, Permutation-adapted complete and independent basis for atomic cluster expansion descriptors, J. Comput. Phys. **510**, 113073 (2024).
51 C. Ma, H. Lei, J. Liang, W. Wu, T. Wang, and D. Fang, Macroscopic mechanical response of chiral-type cylindrical metastructures under axial compression loading, Mater. Des. **158**, 198 (2018).
52 M. Xu, Z. Xu, Z. Zhang, H. Lei, Y. Bai, and D. Fang, Mechanical properties and energy absorption capability of AuxHex structure under in-plane compression: Theoretical and experimental studies, Int. J. Mech. Sci. **159**, 43 (2019).
53 Z. Dong, Y. Li, T. Zhao, W. Wu, D. Xiao, and J. Liang, Experimental and numerical studies on the compressive mechanical properties of the metallic auxetic reentrant honeycomb, Mater. Des. **182**, 108036 (2019).

基于钛晶体的仿原子拉胀超材料设计与优化

周嘉慧, 刘宇航, 邓尊乙, 姜新港, 肖文浩, 余博, 伦应焯, 孟里, 唐刚, 张众, 雷红帅, 侯泽伟, 洪家旺

摘要 与传统材料相比, 拉胀超材料在剪切能力、抗断裂能力和能量吸收方面具有突出的优势, 因此备受关注. 然而, 对于新的拉胀结构缺乏设计灵感. 根据原子晶格材料数据库, 一些天然晶体具有负泊松比. 本文通过密度泛函理论模拟研究了微观尺度钛晶体的拉胀性机理. 然后, 我们通过模仿体心立方钛晶体的微观原子晶格结构, 提出了一种宏观拉胀超材料. 通过理论、数值和实验方法验证了宏观超材料的负泊松比特性. 这种拉胀性在仿钛晶体的宏观超材料中仍然有效, 且具有相似的变形机制. 此外, 从几何参数研究可以知道, 几何参数对宏观超材料的泊松比和杨氏模量有很大的影响. 重要的是, 与初始结构相比, 优化后的超材料拉胀性提高到2倍, 相对杨氏模量提高到25倍. 这项研究在微纳尺度的物理性质和宏观结构之间建立了联系, 为高承载拉胀超材料的设计提供了灵感.